# Morphology-Invariant Metallic Nanoparticles with Tunable Plasmonic Properties

Zhuangqiang Gao,[†,‡] Shikuan Shao,[†] Weiwei Gao,[†] Dianyong Tang,[ǁ] Dianping Tang,[‡] Shengli Zou,[†] Moon J. Kim,[£] and Xiaohu Xia[†,§,*]

[†]*Department of Chemistry, University of Central Florida, Orlando, Florida 32816, United States;*

[‡]*Key Laboratory of Analytical Science for Food Safety and Biology (MOE & Fujian Province), Department of Chemistry, Fuzhou University, Fuzhou 350108, People's Republic of China;*

[ǁ]*International Academy of Targeted Therapeutics and Innovation, Chongqing University of Arts and Sciences, Chongqing 402160, People's Republic of China;*

[§]*NanoScience Technology Center, University of Central Florida, Orlando, Florida 32816, United States;*

[£]*Department of Materials Science and Engineering, University of Texas at Dallas, Richardson, Texas 75080, United States.*

[*]*Corresponding author. E-mail: Xiaohu.Xia@ucf.edu*

## Abstract

Current methods for tuning the plasmonic properties of metallic nanoparticles typically rely on alternating the morphology (*i.e.*, size and/or shape) of nanoparticles. The variation of morphology of plasmonic nanoparticles oftentimes impairs their performance in certain applications. In this study, we report an effective approach based on the control of internal structure to engineer morphology-invariant nanoparticles with tunable plasmonic properties. Specifically, these nanoparticles were prepared through selective growth of Ag on the inner surfaces of preformed Ag-Au alloyed nanocages as the seeds to form Ag@(Ag-Au) shell@shell nanocages. Plasmonic properties of the Ag@(Ag-Au) nanocages can be conveniently and effectively tuned by varying the amount of Ag deposited on the inner surfaces, during which the overall morphology of the nanocages remains unchanged. To demonstrate the potential applications of the Ag@(Ag-Au) nanocages, they were applied to colorimetric sensing of human carcinoembryonic antigen (CEA) that achieved low detection limits. This work provides a meaningful concept to design and craft plasmonic nanoparticles.


## Table of Contents

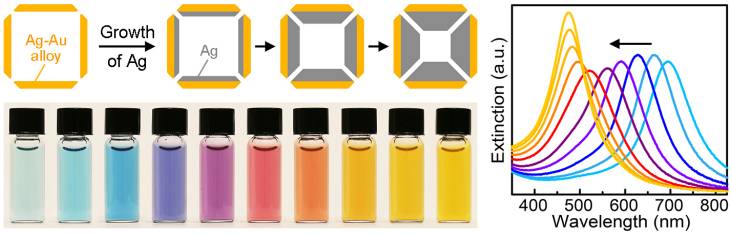



**Keywords:** plasmonics; nanoparticle; metal; controlled synthesis; biosensing

Over the past half-century, metallic nanoparticles with plasmonic properties that arise from a phenomenon called localized surface plasmon resonance (LSPR[1-6]) have been a class of important functional materials. They have found widespread uses in various areas of technology such as sensing,[6-10] biomedicine,[11-14] solar energy harvesting,[15-19] surface-enhanced spectroscopies,[20,21] and electronics.[22,23] The tunability of LSPR properties is crucial for a plasmonic nanoparticle to achieve optimal performance in certain applications. In colorimetric sensing, for example, to ensure a sensitive detection, nanoparticles are expected to be able to display various colors in response to analytes of different concentrations.[8-10] In solar energy conversion, in order to maximize the utilization efficiency of solar light, nanoparticles are engineered to absorb light in broad wavelengths ranging from the visible to infrared regions.[15-19]

Current methods for tuning the LSPR properties of a metallic nanoparticle typically rely on alternating particle morphology, including size and/or shape. Notable examples include size-,[24,25] shape-,[2,11,26] aspect ratio (*e.g.*, nanorods and nanoplates[23,27,28])-, and branch (*e.g.*, nanostars[29,30])-dependent LSPR studies. In practical applications, however, it's often desirable to keep the morphology of a nanoparticle unchanged while tuning its LSPR properties. For instance, in biomedicine, it is well known that the efficiencies of cellular uptake and blood circulation of nanoparticles have a strong dependence on particle size and shape.[31-36] To avoid unexpected side effects, it's ideal to utilize plasmonic nanoparticles with the same morphologies in different sets of experiments. In plasmonic sensing, nanoparticles with different plasmon wavelengths but similar scattering intensities are particularly desired for multiplex sensing.[37-41] Accordingly, nanoparticles are expected to have similar sizes because scattering intensity is proportional to the sixth power of particle size.[6] In photocatalysis, the stabilities and durations of plasmonic nanoparticles have strong dependence on particle morphology.[15,16] In experimental design, it's preferred to fix nanoparticles in a stable morphology while alter other parameters in order to ensure reliable performance. Despite of these preferences in practical applications, it has been a long-standing challenge to tune the LSPR properties of nanoparticles while hold the particle morphology a constant.

In this study, we demonstrate a robust approach based on the control of internal structure to prepare morphology-invariant metallic nanoparticles with tunable LSPR properties. Specifically, these nanoparticles – Ag@(Ag-Au) shell@shell nanocages – were synthesized by selectively depositing Ag atoms on the inner surfaces of preformed Ag-Au alloyed nanocages as the seeds

(see Figure 1a). By varying the amount of Ag atoms added to the inner surfaces (or the thickness of Ag shell), LSPR properties of the Ag@(Ag-Au) shell@shell nanocages can be effectively tuned. Significantly, during the course of LSPR tuning, the overall morphology of the Ag@(Ag-Au) nanocages remains unchanged. It is worth noting that the strategy of growing Ag inside a nanocage is much more effective in tuning LSPR properties than conventional strategies where Ag is grown on outer surfaces of a nanoparticle. To demonstrate the potential applications of these Ag@(Ag-Au) nanocages, we applied them to sensitive colorimetric sensing of disease biomarkers.

## RESULTS AND DISCUSSION

**Synthesis, Characterizations, and LSPR Properties.** We started with the synthesis of Ag@(Ag-Au) nanocages that was achieved through seed-mediated growth. As the seeds, Ag-Au alloyed nanocages with a truncated cubic shape, ~48 nm in average edge length and ~4 nm in wall thickness (Figures 1b) were first obtained through galvanic replacement between ~42 nm Ag nanocubes (Figure S1b,f) and $HAuCl_4$.[42] We selected these Ag-Au cages as seeds because they display a major LSPR peak at a relatively long wavelength, leaving a broad range for tuning LSPR peaks in the visible light region.[43] In a standard synthesis of the Ag@(Ag-Au) nanocages, an aqueous solution of $AgNO_3$ as a precursor to Ag was added to a mixture containing the 48 nm Ag-Au nanocages as the seeds, poly(vinylpyrrolidone) as a stabilizer, and L-ascorbic acid (AA) as a reductant at room temperature (see details in METHODS). As demonstrated in our recently published work,[44-47] the key to force the deposition of Ag atoms to exclusively occur on inner surfaces of a nanocage was to ensure the rate of surface diffusion for Ag adatoms on outer surfaces is greater than the rate of Ag atom deposition (see Figure 1a), which can be achieved by reducing the reaction kinetics. It should be mentioned that the diffusion of Ag adatoms to inner surface of Ag-Au cage during growth (Figure 1a) is driven by thermodynamics since the growth of Ag on the inner surfaces of growing cages can reduce their surface areas and thereby minimize the system total free energy.[45] By controlling the amount of $AgNO_3$, the thickness of Ag shell inside the Ag-Au cages can be conveniently controlled. As representative examples, Figures 1c,d and S2b,c show transmission electron microscopy (TEM) images of two Ag@(Ag-Au) nanocage samples obtained from a standard synthesis when 8.0 and 16.0 μL of $AgNO_3$ solution were added to the reaction. It can be observed that the truncated cubic shape and 48 nm size of the initial Ag-

Au cages as seeds were well preserved after the growth of Ag, suggesting the exclusive inside growth of Ag on the seeds. The Ag shells (with a slightly brighter contrast) inside the Ag-Au cages can be resolved from the TEM images, especially the high-magnification images (Figure 1e-g). Such elemental distributions of Ag and Au were further validated by energy-dispersive X-ray (EDX) mapping and scanning data shown in Figure 1h,i. The thicknesses of Ag shell (see Figure S3 for the definition of Ag shell thickness) of the two samples in Figure 1c,d were measured to be 3.5 ± 0.7 and 10.0 ± 2.7 nm, respectively, by randomly analyzing 200 particles for each sample.

To validate the proposed growth mechanism shown in Figure 1a, we increased the rate of Ag atom deposition by increasing the concentration of AA from 0.4 mM in a standard synthesis to 200 mM, while kept all other conditions unchanged. In this case, if the proposed mechanism is reasonable, growth of Ag on outer surfaces of Ag-Au cages is expected. As indicated by Figure S4, the nanocrystals obtained were indeed Ag@(Ag-Au)@Ag triple walled cages that resulted from the growth of Ag on both outer and inner surfaces of initial Ag-Au cages as seeds. It should be noted that, in addition to the factors of diffusion and deposition as illustrated in Figure 1a, lattice mismatch between Ag and Au may play an important role in the growth mode of Ag on Ag-Au cages as seeds. Specifically, the Ag-Au cages have Au-rich outer surfaces and Ag-rich inner surfaces.[42,48] The newly formed Ag atoms resulted from the reduction of $Ag^+$ ions by AA are expected to prefer to deposit on the Ag-rich inner surfaces because there is no lattice mismatch in Ag-Ag deposition. Such a preferential deposition of Ag in inner surfaces further promotes the formation of Ag@(Ag-Au) cages as final products. This assumption of lattice mismatch is supported by the results that, when $Ag^+$ ions were replaced by $Au^{3+}$ ions, the reduction of $Au^{3+}$ ions led to selective deposition of Au on the Au-rich outer surfaces of Ag-Au cages, resulting in the formation of (Ag-Au)@Au nanocages as final products (see Figure S5).

LSPR properties of the Ag@(Ag-Au) cages with different thicknesses of Ag shell ($t_{Ag}$) were evaluated. Figure 1j shows photographs of aqueous suspensions of different Ag@(Ag-Au) cages ($t_{Ag}$ = 0-10.0 nm) at the same particle concentration that were obtained from the standard synthesis when different amount of $AgNO_3$ was introduced to the reaction. As the thickness of Ag shell ($t_{Ag}$) increased, the color of cage suspensions changed dramatically. The distinct change of colors from cyan to blue, violet, magenta, red, orange, and yellow can be distinguished by the naked eye, making these cages extremely suitable for high-resolution colorimetric sensing.

Along with the color change, continuous blue shift of LSPR peaks (from ~695 to ~475 nm) for these cage suspensions were observed (Figure 1k). Notably, the LSPR peaks well separated each other and the bandwidths of the peaks were similar, which are preferred features in multiplex colorimetric and plasmonic sensing.[8,37-41] It is worth mentioning that the major LSPR peak of the Ag@(Ag-Au)@Ag triple walled cages shown in Figure S4a is located at a longer wavelength ($\lambda_{max} \approx 505$ nm, see Figure S4c) compared to that of the Ag@(Ag-Au) cages with the same amount of deposited Ag ($\lambda_{max} \approx 475$ nm, Figure 1d,k). This observation suggests that selective deposition of Ag on inner surfaces of Ag-Au cages is a highly efficient approach for tuning the LSPR properties. Altogether, these results demonstrate the strong tunability of LSPR properties for the Ag@(Ag-Au) cages.

**Simulations of LSPR Properties.** To gain insights into the tunable LSPR properties of the Ag@(Ag-Au) cages, finite-difference time-domain (FDTD) simulations were performed. Figure 2a shows the geometric models that were set according to the physical parameters and chemical compositions of the Ag@(Ag-Au) cages (see METHODS for details). It should be mentioned that, because the pores in the cages are irregular in terms of numbers, sizes, and locations,[49] pores were not created in the models. Figure 2b shows the simulated extinction cross-section spectra of the Ag@(Ag-Au) cages with different Ag shell thicknesses ($t_{Ag}$) in the range of 0-10 nm. The LSPR peaks gradually blue-shifted from 699 nm to 488 nm as $t_{Ag}$ increased from 0 to 10 nm, a similar trend as what were observed from the experiments (Figure 1k). Similar results were observed when uniform pores of 10 nm in diameter were created in the corners of cage models (see Figure S6). It should be mentioned that the trend of peak intensity change in simulations doesn't align well with the experimental data. This inconsistency might be primarily attributed to the difference in elemental composition on the surface between the models and cages. Specifically, the cages are partially exposing pure Ag on the surface around the pore sites that is more plasmonically active than Au-Ag alloy.[2,50,51] In contrast, the models were constructed with full Ag-Au coverage. To understand the Ag shell thickness ($t_{Ag}$)-dependent LSPR properties, we plotted the locations of major LSPR peaks ($\lambda_{max}$) against $t_{Ag}$. As shown by Figure 2c, the curves generated from simulations and experiments agreed well with each other. As indicated by the electric field intensity enhancement profile of 48 nm Ag@(Ag-Au) cages with $t_{Ag}$ = 10 nm (Figure 2d), the major LSPR peak of the cages was identified to be dipolar plasmon mode. Taken together, both the experimental and simulation results demonstrate the Ag@(Ag-Au) cages could

display tunable LSPR properties at the same overall morphology.

**Size Control.** The size of Ag@(Ag-Au) cages can be conveniently controlled by using Ag-Au cages of different sizes as the initial seeds. As shown by Figures 3a-f and S7, ~27, ~68, and ~113 nm Ag@(Ag-Au) cages with good uniformities were successfully synthesized when Ag-Au cages of the same sizes were used as the seeds for Ag growth. Similar to the ~48 nm Ag@(Ag-Au) cages displayed in Figure 1, Ag was exclusively grown inside all the seeds during the synthesis regardless of the seed size. As a result, the Ag@(Ag-Au) cages produced from each type of seeds had the same size and shape, but different thicknesses of inner Ag shells ($t_{Ag}$). The $t_{Ag}$ of the 27, 68, and 113 nm Ag@(Ag-Au) cages in Figure 3d-f were measured to be 8.8 ± 3.0, 15.9 ± 5.7, and 16.0 ± 7.3 nm, respectively. As shown by Figure 3g-i, the major LSPR peaks ($\lambda_{max}$) of all the three types of Ag@(Ag-Au) cages can be effectively tuned in the visible region by varying $t_{Ag}$. It should be mentioned that the LSPR tunability of 113 nm Ag@(Ag-Au) cages is not as good as the smaller ones ($\lambda_{max}$ = 790-597 nm *versus* 742-483 and 680-447 nm and for 68 and 27 nm cages, respectively). This observation might be related to the fact that, compared to smaller Ag-Au cages, growth of certain amount of Ag inside 113 nm Ag-Au cages has less impact on the change of their degree of hollowness because the space of hollow interior of 113 nm cages is much greater than those of smaller cages. The FDTD-simulated LSPR peaks (see Figures S8-S10) are in good agreement with the experimental results. It is worth noting that, as shown by Figures S8d, S9d, and S10d, the major LSPR peaks for all cages of different sizes were stemmed from dipolar plasmon mode, while the shoulder peaks for 113 nm cages was originated from quadrupolar plasmon mode (Figure S10d). According to our simulation results (see Figure S11), quadrupolar plasmon mode becomes evident when the edge length of Ag@(Ag-Au) cages reaches ~100 nm.

**Comparison with Other Systems.** It should be emphasized that our strategy of growing Ag inside a seed is highly efficient in tuning LSPR properties. In conventional overgrowth-based systems, the strategy was to grow Ag on the outer surfaces of a seed.[51,52] To compare the efficiencies of these two different strategies in tuning LSPR properties, we designed a set of experiments. Specifically, ~58 nm Au nanospheres (Figure S12a) and ~37×90 nm Au nanorods (Figure S13a) that have similar surface areas as the inner surfaces of 48 nm Ag-Au cages (Figure 1b) and similar volume equivalent diameters (which is defined as the diameter for a sphere with the same volume as a particle with a non-spherical shape[53,54]) as the cages were prepared. These

three types of seeds with similar extinction intensities were grown with the same amounts of Ag through the reduction of $AgNO_3$ by AA (see details in Figure 4a and METHODS). The amounts of Ag atoms [in a unit of nanomole (nmol)] deposited on the seeds were quantified by inductively coupled plasma-mass spectrometry (ICP-MS). The changes of color and LSPR peaks at various amounts of deposited Ag atoms (0-16 nmol) were monitored. As shown by the TEM images in Figures S12b, S13b, and S14, at 16 nmol of Ag deposition, Ag shells on or inside the Au spheres, Au rods, and Ag-Au cages could be clearly seen, suggesting successful overgrowth of Ag. It's clear that the growth of Ag inside cages induced much sensitive color change than growth of Ag on the other two types of seeds (Figure 4b-d), which is consistent with the LSPR peak shifts (Figure 4e-g). For better comparisons, $\lambda_{max}$ of the LSPR peaks was plotted against the amounts of deposited Ag atoms (Figure 4h). Among the three cases, inside growth of Ag in Ag-Au cages displayed a much broader linear range with a greater slope (Figure 4i). Notably, the changes of LSPR peaks for growth of Ag on the different seeds were in good agreement with the simulation data (see Figures 4j, 2b, S15, and S16).

To gain more insight into the wide tunability of LSPR peaks of the Ag@(Ag-Au) shell@shell cage system, we performed more simulations using two different models. In the first model, we constructed a Ag@(Ag-Au) core@shell nanoparticle system that has 4 nm Ag-Au shells (the same thickness as the Ag-Au shells in 48 nm Ag@(Ag-Au) shell@shell cages) and solid Ag cores of varying diameters in the range of 24-45 nm (Figure S17a), and calculated their LSPR properties. As shown by Figure S17b, the LSPR tunability of Ag@(Ag-Au) nanoparticle system is much narrower than that of Ag@(Ag-Au) cage system. This observation implies that shell@shell morphology of the Ag@(Ag-Au) cages is partially responsible for their wide tunability of LSPR peaks. In the second model, we constructed a (Ag-Au)@Ag core@shell nanoparticle system that has solid Ag-Au cores of 58 nm in diameter (the same size as the Au spherical cores in Figure 4) and Ag shells of varying thicknesses in the range of 0-10 nm (Figure S18a). The simulation results (Figure S18b) show that, as the thickness of Ag shell increases, only slightly red shifts are observed for the major LSPR peaks of the (Ag-Au)@Ag nanoparticles. This observation further demonstrates that our strategy of growing Ag inside Ag-Au cages is highly efficient in tuning LSPR properties.

**Application in Biosensing.** Finally, we demonstrated the applications of the Ag@(Ag-Au) cages in biosensing. Human carcinoembryonic antigen (CEA, a cancer biomarker[55,56]) as a model

analyte was detected according to the principle shown in Figure 5a (see METHODS for details). The main idea is that CEA is specifically captured by antibodies labeled with alkaline phosphatase (ALP) – an enzyme that can catalyze the formation of AA to activate the growth of Ag inside Ag-Au cages.[57,58] As such, detection of CEA can be achieved by either monitoring the color change of reaction solution by the naked eye (for semiquantitative analysis) or quantifying the LSPR peak changes with a UV-vis spectrophotometer (for quantitative analysis). CEA standards with various concentrations were detected with this Ag@(Ag-Au) cages-based sensor. A digital camera was used to record the detection results (Figure 5b). A set of different colors were observed at different concentrations of CEA. Using the blank of 0 ng $mL^{-1}$ CEA (cyan color) as a reference, the detection limit by the naked eye was ~2 ng $mL^{-1}$, which is lower than the threshold of CEA level in normal human serum (2.5-5.0 ng $mL^{-1}$).[55,56] Figure 5c shows typical LSPR extinction spectra recorded from the assay solutions at different CEA concentrations. A calibration curve was obtained by plotting the shift of $\lambda_{max}$ relative to the blank ($\Delta\lambda_{max}$) against CEA concentration (Figure 5d). A good linear relationship ($R^2$ = 0.998) was observed in 0.5-15 ng $mL^{-1}$ CEA (Figure 5e). The limit of detection (LOD, which is defined by the 3SD method[59,60]) was determined to be 0.14 ng $mL^{-1}$. Notably, this LOD is approximately 3 times lower than the LOD of conventional ALP-based enzyme-linked immunosorbent assay (ELISA) that uses the same set of antibodies and similar procedure as the Ag@(Ag-Au) cages-based sensor (see Figure S19 for details). The coefficient of variations (CVs) in the entire CEA concentration range were ≤14.7% ($n$ = 6), suggesting a good reproducibility.

To demonstrate the potential clinical uses, we applied the Ag@(Ag-Au) cages-based sensor for detecting human plasma samples (CEA free, purchased from Millipore Sigma) that were spiked with CEA of five different concentrations in the range of 2-100 ng $mL^{-1}$. CEA in each sample was visually semi-quantified and instrumentally quantified based on the color chart and the calibration curve shown in Figures 5b and 5e, respectively. As summarized in Table 1, for semi-quantitative analysis, the CEA concentrations in the five samples could be estimated precisely according to the colors of the corresponding assay solutions. For quantitative analysis, analytical recoveries[61] for the five samples were determined to be 93.0-107.6%, along with CVs ≤12.6% ($n$ = 3). These results indicate that the performance of Ag@(Ag-Au) cages in biosensing was not significantly influenced by the complex matrices of human plasma, implying the potential practical uses in clinical settings.

## CONCLUSIONS

In summary, we have demonstrated an approach based on the control of internal structure to engineer plasmonic nanoparticles made of Ag and Au. Such plasmonic nanoparticles feature invariant morphologies, highly active and tunable plasmonic activities, and adjustable sizes. A potential application of the plasmonic nanoparticles was demonstrated through sensitive colorimetric immunoassay of cancer biomarker. The concept of internal structure control may be extended to other plasmonic nanocrystals of different materials. This work provides an effective method to design and synthesize plasmonic nanomaterials for various basic and applied research.

## METHODS

**Chemicals and Materials.** Silver nitrate ($AgNO_3$, ≥99.0%), gold(III) chloride trihydrate ($HAuCl_4 \cdot 3H_2O$, ≥99.9%), poly(vinylpyrrolidone) (PVP, $M_w \approx 55000$), sodium hydrosulfide hydrate ($NaHS \cdot xH_2O$), L-ascorbic acid (AA, ≥99%), sodium citrate dihydrate (≥99%), sodium borohydride (≥98%), diethanolamine (DEA, ≥98%), nitric acid ($HNO_3$, 70%), hydrochloric acid (HCl, 37%), magnesium nitrate hexahydrate [$Mg(NO_3)_2 \cdot 6H_2O$, 99%], hexadecyltrimethylammonium bromide (CTAB, ≥98%), alkaline phosphatase from bovine intestinal mucosa, L-ascorbic acid 2-phosphate (AA-P) sesquimagnesium salt hydrate (≥95%), 4-nitrophenyl phosphate (pNPP) disodium salt hexahydrate (≥99%), bovine serum albumin (BSA, ≥98%), human carcinoembryonic antigen (CEA, ≥99%), sodium carbonate ($Na_2CO_3$, ≥99.5%), sodium bicarbonate ($NaHCO_3$, ≥99.7%), potassium phosphate monobasic ($KH_2PO_4$, ≥99%), sodium phosphate dibasic ($Na_2HPO_4$, ≥99%), sodium chloride (NaCl, ≥99.5%), potassium chloride (KCl, ≥99%), and Tween 20 were all obtained from Millipore Sigma. Ethylene glycol (EG) was obtained from J. T. Baker. Polyclonal rabbit anti-human CEA antibody (rabbit anti-CEA pAb) and monoclonal mouse anti-human CEA antibody (mouse anti-CEA mAb) were obtained from Abcam plc. ALP-labeled goat anti-mouse IgG antibody was purchased from Thermo Fisher Scientific, Inc. High-binding 96-well microtiter plates (No. 655061) were obtained from Greiner Bio-One. Deionized (DI) water with a resistivity of 18.2 MΩ·cm was used to prepare all aqueous solutions.

**Preparation of Ag Nanocubes To Be Used as Sacrificial Templates.** *Ag cubes of ~25 and ~42 nm in edge length.* These two Ag cubes (samples in Figure S1a,b,e,f) were prepared according to a previously reported one-pot synthesis with minor changes.[42,62] In brief, 6.0 mL of EG was hosted in a glass vial and was heated in an oil bath pre-set to 150 °C under magnetic stirring. After 1 h of preheating, 80 μL of NaHS solution (3.0 mM, in EG), 1500 μL of PVP solution (20 mg/mL, in EG), and 500 μL of $AgNO_3$ solution (48 mg/mL, in EG) were in turn added with a pipette. After the vial had been capped, the reaction was allowed to proceed for different periods of time at 150 °C. The 25 and 42 nm Ag cubes were obtained by quenching the reaction with an ice-water bath when the reaction had been proceeded for 4 and 10 min, respectively. The Ag cubes were

collected by washing with acetone once and DI water for three times *via* centrifugation and dispersed in 4.0 mL DI water.

*Ag cubes of ~61 and ~103 nm in edge length.* These two Ag cubes (samples in Figure S1c,d,g,h) were prepared according to previously published procedures with some modifications,[25,63] where the aforementioned 42 nm Ag cubes were utilized as the seeds. Before synthesis, the 42 nm Ag cubes (1.0 mL) was centrifuged to remove water and then redispersed in 1.0 mL of EG. In a typical synthesis, 3.0 mL of EG was added to a glass vial and was then preheated in an oil bath pre-set to 150 °C under magnetic stirring for 20 min. Thereafter, 900 μL of PVP solution (20 mg/mL, in EG), 200 μL of the 42 nm Ag cubes (in EG), and 600 μL of $AgNO_3$ solution (36 mg/mL, in EG) were added in sequence with a pipette. During this synthesis process, the vial was capped with a vial cap except during the addition of the reaction reagents. The 61 and 103 nm Ag cubes were obtained by stopping the reaction using an ice-water bath once the reaction mixture reached a major LSPR extinction peak around 480 and 585 nm, respectively. After being washed with acetone once and DI water for three times, the Ag cubes were dispersed in 4.0 mL DI water.

The exact edge lengths of abovementioned four Ag cubes were measured to be 25.3 ± 1.2 nm, 42.1 ± 2.1 nm, 61.1 ± 3.0 nm, and 102.8 ± 4.9 nm, respectively, according to their TEM images (Figure S1).

**Preparation of Ag-Au Nanocages To Be Used as Seeds.** *Ag-Au cages of ~48 nm in edge length.* The 48 nm Ag-Au cages (sample shown in Figure 1b) were prepared based on the galvanic replacement reaction between the 42 nm Ag cubes as the sacrificial templates (sample shown in Figure S1b,f) and $HAuCl_4$, according to a published procedure with minor changes.[42] Briefly, 0.5 mL of 42 nm Ag cubes (in DI water) and 9.5 mL of PVP aqueous solution (0.2%, w/v) were placed in a 25-mL flask and were then preheated for 10 min in an oil bath pre-set to 100 °C under magnetic stirring. Thereafter, a $HAuCl_4$ aqueous solution (0.02%, w/v) was added to the flask using a syringe pump at an injection rate of 6.0 mL/h. The 48 nm Ag-Au cages were obtained by terminating the introduction of $HAuCl_4$ when the reaction suspension had displayed a cyan color with a major LSPR extinction peak at ~695 nm. The 48 nm Ag-Au cages were washed with saturated NaCl aqueous solution for one time and with DI water for more than 10 times, and eventually dispersed in 1.0 mL DI water for future use.

*Ag-Au cages of ~27, ~68, and ~113 nm in edge lengths.* The procedures for the syntheses of 27, 68, and 113 nm Ag-Au cages (samples shown in Figure 3a-c) were the same as the procedure for 48 nm Ag-Au cages except that 1.0 mL of 25, 61, and 103 nm Ag cubes, respectively, were used as the sacrificial templates. The 27, 68, and 113 nm Ag-Au cages were obtained by terminating the introduction of $HAuCl_4$ when the reaction suspension had reached major LSPR extinction peaks at ~680, ~742, and ~790 nm, respectively.

The exact edge lengths and thicknesses of abovementioned four Ag-Au cages were measured to be 26.8 ± 1.6, 47.9 ± 2.5, 67.7 ± 3.2, and 113.4 ± 5.1 nm and 2.3 ± 0.2, 3.9 ± 0.3, 6.0 ± 0.4, and 10.6 ± 0.7 nm, respectively, according to their TEM images (Figures 1b, 3a-c, S2a, and S7a-c).

**Synthesis of Ag@(Ag-Au) Nanocages.** *Ag@(Ag-Au) cages of ~48 nm in edge length.* The 48 nm

Ag@(Ag-Au) cages (samples shown in Figure 1c,d,j,k) were prepared by seed-mediated growth method with the above-mentioned 48 nm Ag-Au cages as the seeds, according to our recently reported protocol with some modifications.[47] Prior to synthesis, 200 μL of the 48 nm Ag-Au cages was diluted with DI water to reach an LSPR extinction intensity of 4.00 a.u. at 695 nm, in a cuvette with an optical path length (OPL) of 1 cm. In a standard synthesis, 500 μL of the 48 nm Ag-Au cages (4.00 a.u. at 695 nm, OPL = 1 cm), 1000 μL of 1% (w/v) PVP aqueous solution, and 500 μL of AA solution (0.4 mM, in DI water) were mixed in a flask under magnetic stirring at room temperature, followed by one-shot injection of 10 mM $AgNO_3$ aqueous solution with different volumes. The reaction was allowed to proceed at room temperature for 1 hour. After being washed twice with DI water, the product [*i.e.*, 48 nm Ag@(Ag-Au) cages] was dispersed in 2.0 mL DI water. By varying the volumes of the $AgNO_3$ aqueous solution in the range of 0~16.0 μL, 48 nm Ag@(Ag-Au) cages with different wall thicknesses of Ag inner-shells were obtained.

*Ag@(Ag-Au) cages of ~27, ~68, and ~113 nm in edge length.* The procedures for the syntheses of 27, 68, and 113 nm Ag@(Ag-Au) cages (samples in Figure 3d-i) were the same as the procedure for the 48 nm Ag@(Ag-Au) cages except for using 27, 68, and 113 nm Ag-Au cages as the seeds and varying the volumes of 10 mM $AgNO_3$ aqueous solution in the ranges of 0~22.0, 0~16.0, and 0~28.0 μL, respectively.

**Synthesis of Au Nanospheres with Diameter of ~58 nm.** The ~58 nm Au spheres (sample shown in Figure S12a) were prepared using the Frens' method with minor changes.[64] Briefly, 50 mL of DI water was added to a 100-mL flask equipped with a condenser, and heated to boiling in an oil bath under magnetic stirring. Subsequently, 500 μL of 1% (w/v) $HAuCl_4$ aqueous solution and 550 μL of 1% (w/v) sodium citrate aqueous solution were sequentially added into the boiling water with a pipette. After reacting for 30 min, the 58 nm Au spheres as products were washed with DI water twice and redispersed in 5.0 mL of DI water for future use. The exact diameter of these Au spheres was measured to be 58.1 ± 11.1 nm according to their TEM image (Figure S12a).

**Synthesis of Au Nanorods with Diameter of ~37 nm and Length of ~90 nm.** The 37×90 nm Au rods (sample in Figure S13a) were synthesized using a seed-mediated growth method with minor modifications.[65,66] Briefly, 600 μL of freshly prepared 10 mM $NaBH_4$ aqueous solution was rapidly injected into an 10 mL aqueous solution containing 0.25 mM $HAuCl_4$ and 0.1 M CTAB in a vial at room temperature under magnetic stirring. The mixture was kept undisturbed at 30 °C for 2 hours before use. Subsequently, 9.0 μL of the above mixture was added into a growth solution containing 18.0 mL of 0.1 M CTAB aqueous solution, 900 μL of 10 mM $HAuCl_4$ aqueous solution, 180 μL of 10 mM $AgNO_3$ aqueous solution, 360 μL of 1.0 M HCl aqueous solution, and 144 μL of 100 mM AA aqueous solution. The reaction was proceeded at 30 °C overnight. After being washed twice with DI water, the Au rods as products were stored in 2.0 mL of DI water. The exact diameter and length of these Au rods were measured to be 37.0 ± 3.9 and 89.8 ± 7.1 nm, respectively, according to their TEM image (Figure S13a).

**Growth of Ag on Three Different Types of Nanostructures, Including 48 nm Ag-Au Cages, 58 nm Au**

**Spheres, and 37×90 nm Au Rods.** The growths of Ag on these three types of nanostructures were performed under the same conditions. In a standard procedure of growth, 200 μL of nanostructures was first diluted with DI water in a cuvette with an OPL of 1 cm to reach an extinction intensity of 4.00 a.u. at $\lambda_{max}$ ($\lambda_{max}$ = 695 nm for 48 nm Ag-Au cages; $\lambda_{max}$ = 542 nm for 58 nm Au nanospheres; and $\lambda_{max}$ = 688 nm for 37×90 nm Au rods). Then, 30 μL of AA solution with a specific concentration was added to a suspension containing 50 μL of the diluted Ag/Au nanostructures (4.00 a.u. at $\lambda_{max}$, OPL = 1 cm), 5 μL of aqueous solution of 10% PVP and 2.5 mM CTAB, 20 μL of 1.0 M DEA buffer (pH 9.8), and 5 μL of 10 mM $AgNO_3$ aqueous solution. The mixture was allowed to react for 1 hour at 37 °C. Note, the amount of Ag grown on the nanostructures was controlled by varying the concentration of AA solution. Finally, *i*) 100 μL of the resulting suspension was added into a well of 96-well microtiter plates. A digital camera and a microplate reader were used to take the photograph and record the LSPR extinction spectrum of the suspension, respectively; and *ii*) the nanoparticles in the resulting suspension were collected by centrifugation. Inductively coupled plasma-mass spectrometry (ICP-MS) was used to determine the amounts of Ag and Au elements in the nanoparticles, which could be converted to the amounts of Ag atoms [in a unit of nanomole (nmol)] deposited on the Ag/Au nanostructures.

**Standard Procedure for Colorimetric Detection of CEA Using 48 nm Ag@(Ag-Au) Cages-Based Sensor (see Figure 5a for detection principle).** The 96-well microtiter plates were first coated with 50 μL rabbit anti-CEA pAb (10 μg $mL^{-1}$, in 10 mM carbonate buffer, pH = 9.6) at 4 °C overnight. After being washed with washing solution [10 mM PBS buffer (pH 7.4) containing 0.05% Tween 20, PBST] for five times, the plates were blocked by 300 μL blocking solution (2% BSA in PBST) at 37 °C for 2 h. After the plates had been washed with washing solution for five times, 100 μL CEA standards in dilution solution (1% BSA in PBST) was added to each well. After incubating at 37 °C for 1 h, the plates were washed with washing solution for five times, followed by the addition of 100 μL mouse anti-CEA mAb (1 μg $mL^{-1}$, in dilution solution) to each well. After incubating at 37 °C for 1 h, the plates were washed five times. Then, 100 μL ALP-labeled goat anti-mouse IgG (1 μg $mL^{-1}$, in dilution buffer) was added. The plates were incubated at 37 °C for 1 h. After washing five times, 100 μL freshly prepared substrate solution was added. Here, the substrate solution was prepared by mixing 1000 μL of the 48 nm Ag-Au cages (4.00 a.u. at 695 nm, OPL = 1 cm), 100 μL of 10% PVP and 2.5 mM CTAB mixed aqueous solution, 400 μL of 1.0 M DEA buffer (pH 9.8), 100 μL of 10 mM $AgNO_3$ aqueous solution, and 600 μL of DI water. After 1-hour incubation at 37 °C, the photograph and LSPR extinction spectrum of each well were taken by a digital camera and recorded by a microplate reader, respectively.

Procedure of ALP-based ELISA of CEA (Figure S19) was the same as above standard procedure of 48 nm Ag@(Ag-Au) cages-based sensor except for the use of a different substrate solution. Specifically, after all the immunoreactions, 100 μL of 5 mM pNPP in 1.0 M DEA buffer (pH 9.8) as substrate solution was added to each well. After incubation at 37 °C for 1 hour, the absorbance at 405 nm of each well was measured using a microplate reader.

**Finite-Difference Time-Domain (FDTD) Simulations.** The FDTD simulations were performed on the metal nanostructures including Ag@(Ag-Au) cages, Au@Ag spheres, Au@Ag rods, Ag@(Ag-Au) spheres, and (Ag-Au)@Ag spheres using a commercial software (FDTD Solutions 8.0, Lumerical Solutions, Inc.), using published procedures in the literature with some modifications.[28,51] During the simulations, an electromagnetic pulse in the wavelength range from 300 to 1000 nm was launched into a box containing a target metal nanostructure. A mesh size of 1 nm was employed in calculating the extinction cross-section spectra and electric field intensity enhancements of the metal nanostructures. The refractive index of the surrounding medium was set to 1.33 (*i.e.*, the refractive index of water). The dielectric functions of Ag and Au were obtained from previously measured values.[67,68] For simplicity, the Ag@(Ag-Au) cages were modeled as a hollow cuboctahedron with Ag shell in the inner surface and Ag-Au alloy on the outer surface (see Figures 2a, S8a, S9a, S10a, and S11a). The molar ratio of Ag to Au for the Ag-Au alloy was set to be 2:1 according to experimental data from ICP-MS analysis. The outer edge lengths of the Ag@(Ag-Au) cage ($L_{outer}$), thicknesses of Ag shell ($t_{Ag}$) and Ag-Au alloy layer ($t_{Ag\text{-}Au}$) were set to specific values that were obtained from electron microscope imaging data. For Ag@(Ag-Au) cage of a certain size, the thickness of Ag-Au alloy layer is fixed, while thickness of Ag shell is varied. The Au@Ag spheres were modeled as Au@Ag core@shell spheres. The diameter of Au core and the thickness of Ag shell were set to be 58 nm and 0~10 nm, respectively, according to the electron microscope imaging data (see Figure S12). The Au@Ag rods were modeled as Au@Ag core@shell right circular cylinders. The diameter and length of Au core were set to be 37 and 90 nm, respectively, and the thickness of Ag shell were set to be in the range of 0~10 nm, according to the electron microscope imaging data (see Figure S13). The parameters of all other models in the Supporting Information are provided in the figure captions.

**Characterizations.** A JEOL JEM-1011 microscope was used to take the transmission electron microscope (TEM) images. A FEI 200kV Titan Themis scanning TEM was used to acquire the energy dispersive X-ray (EDX) mapping images and line-scan spectra. A JY2000 Ultrace ICP atomic emission spectrometer was used to determine the amounts of Ag and Au elements in various nanostructures. A Canon EOS Rebel T7 digital camera was used to take the photographs of samples in vials and microtiter plates. An Agilent Cary 60 UV-vis spectrophotometer and a Tecan Infinite 200 PRO microplate reader were used to record the LSPR extinction spectra of samples in vials and microtiter plates, respectively. An Oakton pH 700 benchtop meter was used to measure the pH values of buffers.

## ASSOCIATED CONTENT

### Supporting Information

The Supporting Information is available free of charge on the ACS Publications website at DOI: xxx.

TEM images and LSPR extinction spectra of various nanostructures; schematic models,

simulated extinction cross-section spectra, and electric field intensity enhancement profiles of various Ag@(Ag-Au) cages; schematic models and simulated extinction cross-section spectra of Au@Ag spheres and rods, (Ag-Au)@Ag spheres, and Ag@(Ag-Au) spheres; calibration curve of ALP-based ELISA of CEA.

**Notes**

The authors declare no competing financial interests.

**ACKNOWLEDGMENTS**

This work was supported in part by a National Science Foundation (NSF) grant (DMR-2004546) and startup funds from the University of Central Florida (UCF). Z.G. was supported in part by the Preeminent Postdoctoral Program at UCF. The authors thank P. Mukherjee for his help with electron microscope analyses.

**REFERENCES**

1. Kelly, K. L.; Coronado, E.; Zhao, L. L.; Schatz, G. C. The Optical Properties of Metal Nanoparticles: The Influence of Size, Shape, and Dielectric Environment. *J. Phys. Chem. B* **2003**, *107*, 668-677.
2. Rycenga, M.; Cobley, C. M.; Zeng, J.; Li, W.; Moran, C. H.; Zhang, Q.; Qin, D.; Xia, Y. Controlling the Synthesis and Assembly of Silver Nanostructures for Plasmonic Applications. *Chem. Rev.* **2011**, *111*, 3669-3712.
3. Murphy, C. J.; Chang, H.-H.; Falagan-Lotsch, P.; Gole, M. T.; Hofmann, D. M.; Hoang, K. N. L.; McClain, S. M.; Meyer, S. M.; Turner, J. G.; Unnikrishnan, M.; Wu, M.; Zhang, X.; Zhang, Y. Virus-Sized Gold Nanorods: Plasmonic Particles for Biology. *Acc. Chem. Res.* **2019**, *52*, 2124-2135.
4. Austin, L. A.; Kang, B.; El-Sayed, M. A. Probing Molecular Cell Event Dynamics at the Single-Cell Level with Targeted Plasmonic Gold Nanoparticles: A Review. *Nano Today* **2015**, *10*, 542-558.
5. Halas, N. J.; Lal, S.; Chang, W.-S.; Link, S.; Nordlander, P. Plasmons in Strongly Coupled Metallic Nanostructures. *Chem. Rev.* **2011**, *111*, 3913-3961.
6. Mayer, K. M.; Hafner, J. H. Localized Surface Plasmon Resonance Sensors. *Chem. Rev.*

**2011**, *111*, 3828-3857.

7. Tokel, O.; Inci, F.; Demirci, U. Advances in Plasmonic Technologies for Point of Care Applications. *Chem. Rev.* **2014**, *114*, 5728-5752.
8. Tang, L.; Li, J. Plasmon-Based Colorimetric Nanosensors for Ultrasensitive Molecular Diagnostics. *ACS Sens.* **2017**, *2*, 857-875.
9. Zhang, Z.; Wang, H.; Chen, Z.; Wang, X.; Choo, J.; Chen, L. Plasmonic Colorimetric Sensors Based on Etching and Growth of Noble Metal Nanoparticles: Strategies and Applications. *Biosens. Bioelectron.* **2018**, *114*, 52-65.
10. Ma, X.; He, S.; Qiu, B.; Luo, F.; Guo, L.; Lin, Z. Noble Metal Nanoparticle-Based Multicolor Immunoassays: An Approach toward Visual Quantification of the Analytes with the Naked Eye. *ACS Sens.* **2019**, *4*, 782-791.
11. Dreaden, E. C.; Alkilany, A. M.; Huang, X.; Murphy, C. J.; El-Sayed, M. A. The Golden Age: Gold Nanoparticles for Biomedicine. *Chem. Soc. Rev.* **2012**, *41*, 2740-2779.
12. D. Howes, P.; Rana, S.; M. Stevens, M. Plasmonic Nanomaterials for Biodiagnostics. *Chem. Soc. Rev.* **2014**, *43*, 3835-3853.
13. Zhou, W.; Gao, X.; Liu, D.; Chen, X. Gold Nanoparticles for *in Vitro* Diagnostics. *Chem. Rev.* **2015**, *115*, 10575-10636.
14. Yang, X.; Yang, M.; Pang, B.; Vara, M.; Xia, Y. Gold Nanomaterials at Work in Biomedicine. *Chem. Rev.* **2015**, *115*, 10410-10488.
15. Yang, J.; Guo, Y.; Lu, W.; Jiang, R.; Wang, J. Emerging Applications of Plasmons in Driving $CO_2$ Reduction and $N_2$ Fixation. *Adv. Mater.* **2018**, *30*, 1802227.
16. Zhang, Z.; Zhang, C.; Zheng, H.; Xu, H. Plasmon-Driven Catalysis on Molecules and Nanomaterials. *Acc. Chem. Res.* **2019**, *52*, 2506-2515.
17. Linic, S.; Aslam, U.; Boerigter, C.; Morabito, M. Photochemical Transformations on Plasmonic Metal Nanoparticles. *Nat. Mater.* **2015**, *14*, 567-576.
18. Jang, Y. H.; Jang, Y. J.; Kim, S.; Quan, L. N.; Chung, K.; Kim, D. H. Plasmonic Solar Cells: From Rational Design to Mechanism Overview. *Chem. Rev.* **2016**, *116*, 14982-15034.
19. Ueno, K.; Oshikiri, T.; Sun, Q.; Shi, X.; Misawa, H. Solid-State Plasmonic Solar Cells. *Chem. Rev.* **2018**, *118*, 2955-2993.
20. Li, J.-F.; Zhang, Y.-J.; Ding, S.-Y.; Panneerselvam, R.; Tian, Z.-Q. Core–Shell Nanoparticle-Enhanced Raman Spectroscopy. *Chem. Rev.* **2017**, *117*, 5002-5069.

21. Li, J.-F.; Li, C.-Y.; Aroca, R. F. Plasmon-Enhanced Fluorescence Spectroscopy. *Chem. Soc. Rev.* **2017**, *46*, 3962-3979.
22. Ozbay, E. Plasmonics: Merging Photonics and Electronics at Nanoscale Dimensions. *Science* **2006**, *311*, 189-193.
23. Chen, H.; Shao, L.; Li, Q.; Wang, J. Gold Nanorods and Their Plasmonic Properties. *Chem. Soc. Rev.* **2013**, *42*, 2679-2724.
24. Ruan, Q.; Shao, L.; Shu, Y.; Wang, J.; Wu, H. Growth of Monodisperse Gold Nanospheres with Diameters from 20 nm to 220 nm and Their Core/Satellite Nanostructures. *Adv. Opt. Mater.* **2014**, *2*, 65-73.
25. Zhang, Q.; Li, W.; Moran, C.; Zeng, J.; Chen, J.; Wen, L.-P.; Xia, Y. Seed-Mediated Synthesis of Ag Nanocubes with Controllable Edge Lengths in the Range of 30−200 nm and Comparison of Their Optical Properties. *J. Am. Chem. Soc.* **2010**, *132*, 11372-11378.
26. Orendorff, C. J.; Sau, T. K.; Murphy, C. J. Shape-Dependent Plasmon-Resonant Gold Nanoparticles. *Small* **2006**, *2*, 636-639.
27. Millstone, J. E.; Hurst, S. J.; Métraux, G. S.; Cutler, J. I.; Mirkin, C. A. Colloidal Gold and Silver Triangular Nanoprisms. *Small* **2009**, *5*, 646-664.
28. Qin, F.; Zhao, T.; Jiang, R.; Jiang, N.; Ruan, Q.; Wang, J.; Sun, L.-D.; Yan, C.-H.; Lin, H.-Q. Thickness Control Produces Gold Nanoplates with Their Plasmon in the Visible and Near-Infrared Regions. *Adv. Opt. Mater.* **2016**, *4*, 76-85.
29. Rodríguez-Lorenzo, L.; Romo-Herrera, J. M.; Pérez-Juste, J.; Alvarez-Puebla, R. A.; Liz-Marzán, L. M. Reshaping and LSPR Tuning of Au Nanostars in the Presence of CTAB. *J. Mater. Chem.* **2011**, *21*, 11544-11549.
30. Rodríguez-Lorenzo, L.; de la Rica, R.; Álvarez-Puebla, R. A.; Liz-Marzán, L. M.; Stevens, M. M. Plasmonic Nanosensors with Inverse Sensitivity by Means of Enzyme-Guided Crystal Growth. *Nat. Mater.* **2012**, *11*, 604-607.
31. Cho, E. C.; Zhang, Q.; Xia, Y. The Effect of Sedimentation and Diffusion on Cellular Uptake of Gold Nanoparticles. *Nat. Nanotechnol.* **2011**, *6*, 385-391.
32. Chithrani, B. D.; Chan, W. C. W. Elucidating the Mechanism of Cellular Uptake and Removal of Protein-Coated Gold Nanoparticles of Different Sizes and Shapes. *Nano Lett.* **2007**, *7*, 1542-1550.
33. Wang, Y.; Black, K. C. L.; Luehmann, H.; Li, W.; Zhang, Y.; Cai, X.; Wan, D.; Liu, S.-Y.; Li,

M.; Kim, P.; Li, Z.-Y.; Wang, L. V.; Liu, Y.; Xia, Y. Comparison Study of Gold Nanohexapods, Nanorods, and Nanocages for Photothermal Cancer Treatment. *ACS Nano* **2013**, *7*, 2068-2077.

34. Davis, M. E.; Chen, Z.; Shin, D. M. Nanoparticle Therapeutics: An Emerging Treatment Modality for Cancer. *Nat. Rev. Drug Discov.* **2008**, *7*, 771-782.
35. Ali, M. R. K.; Wu, Y.; El-Sayed, M. A. Gold-Nanoparticle-Assisted Plasmonic Photothermal Therapy Advances toward Clinical Application. *J. Phys. Chem. C* **2019**, *123*, 15375-15393.
36. Abadeer, N. S.; Murphy, C. J. Recent Progress in Cancer Thermal Therapy Using Gold Nanoparticles. *J. Phys. Chem. C* **2016**, *120*, 4691-4716.
37. Hu, R.; Yong, K.-T.; Roy, I.; Ding, H.; He, S.; Prasad, P. N. Metallic Nanostructures as Localized Plasmon Resonance Enhanced Scattering Probes for Multiplex Dark-Field Targeted Imaging of Cancer Cells. *J. Phys. Chem. C* **2009**, *113*, 2676-2684.
38. Wang, C.; Irudayaraj, J. Gold Nanorod Probes for the Detection of Multiple Pathogens. *Small* **2008**, *4*, 2204-2208.
39. Kim, H.; Lee, J. U.; Song, S.; Kim, S.; Sim, S. J. A Shape-Code Nanoplasmonic Biosensor for Multiplex Detection of Alzheimer's Disease Biomarkers. *Biosens. Bioelectron.* **2018**, *101*, 96-102.
40. Sciacca, B.; Monro, T. M. Dip Biosensor Based on Localized Surface Plasmon Resonance at the Tip of an Optical Fiber. *Langmuir* **2014**, *30*, 946-954.
41. Hildebrandt, N. Biofunctional Quantum Dots: Controlled Conjugation for Multiplexed Biosensors. *ACS Nano* **2011**, *5*, 5286-5290.
42. Skrabalak, S. E.; Au, L.; Li, X.; Xia, Y. Facile Synthesis of Ag Nanocubes and Au Nanocages. *Nat. Protoc.* **2007**, *2*, 2182-2190.
43. Skrabalak, S. E.; Chen, J.; Sun, Y.; Lu, X.; Au, L.; Cobley, C. M.; Xia, Y. Gold Nanocages: Synthesis, Properties, and Applications. *Acc. Chem. Res.* **2008**, *41*, 1587-1595.
44. Xia, X.; Xie, S.; Liu, M.; Peng, H.-C.; Lu, N.; Wang, J.; Kim, M. J.; Xia, Y. On the Role of Surface Diffusion in Determining the Shape or Morphology of Noble-Metal Nanocrystals. *Proc. Natl. Acad. Sci. U. S. A.* **2013**, *110*, 6669-6673.
45. Xia, Y.; Xia, X.; Peng, H.-C. Shape-Controlled Synthesis of Colloidal Metal Nanocrystals: Thermodynamic *Versus* Kinetic Products. *J. Am. Chem. Soc.* **2015**, *137*, 7947-7966.
46. Ye, H.; Wang, Q.; Catalano, M.; Lu, N.; Vermeylen, J.; Kim, M. J.; Liu, Y.; Sun, Y.; Xia, X.

Ru Nanoframes with an *fcc* Structure and Enhanced Catalytic Properties. *Nano Lett.* **2016**, *16*, 2812-2817.

47. Gao, Z.; Ye, H.; Wang, Q.; Kim, M. J.; Tang, D.; Xi, Z.; Wei, Z.; Shao, S.; Xia, X. Template Regeneration in Galvanic Replacement: A Route to Highly Diverse Hollow Nanostructures. *ACS Nano* **2020**, *14*, 791-801.
48. Moreau, L. M.; Schurman, C. A.; Kewalramani, S.; Shahjamali, M. M.; Mirkin, C. A.; Bedzyk, M. J. How Ag Nanospheres Are Transformed into AgAu Nanocages. *J. Am. Chem. Soc.* **2017**, *139*, 12291-12298.
49. Xia, X.; Wang, Y.; Ruditskiy, A.; Xia, Y. 25th Anniversary Article: Galvanic Replacement: A Simple and Versatile Route to Hollow Nanostructures with Tunable and Well-Controlled Properties. *Adv. Mater.* **2013**, *25*, 6313-6333.
50. Gao, C.; Hu, Y.; Wang, M.; Chi, M.; Yin, Y. Fully Alloyed Ag/Au Nanospheres: Combining the Plasmonic Property of Ag with the Stability of Au. *J. Am. Chem. Soc.* **2014**, *136*, 7474-7479.
51. Jiang, R.; Chen, H.; Shao, L.; Li, Q.; Wang, J. Unraveling the Evolution and Nature of the Plasmons in (Au Core)–(Ag Shell) Nanorods. *Adv. Mater.* **2012**, *24*, OP200-OP207.
52. Samal, A. K.; Polavarapu, L.; Rodal-Cedeira, S.; Liz-Marzán, L. M.; Pérez-Juste, J.; Pastoriza-Santos, I. Size Tunable Au@Ag Core–Shell Nanoparticles: Synthesis and Surface-Enhanced Raman Scattering Properties. *Langmuir* **2013**, *29*, 15076-15082.
53. Grassian, V. H. When Size Really Matters: Size-Dependent Properties and Surface Chemistry of Metal and Metal Oxide Nanoparticles in Gas and Liquid Phase Environments. *J. Phys. Chem. C* **2008**, *112*, 18303-18313.
54. Tian, L.; Ahmadi G.; Tu, J. Mobility of Nanofiber, Nanorod, and Straight-Chain Nanoparticles in Gases. *Aerosol Sci. Technol.* **2017**, *51*, 587-601.
55. Lawler, M.; Johnston, B.; Van Schaeybroeck, S.; Salto-Tellez, M.; Wilson, R.; Dunlop, M.; Johnston, P. G., 74 - Colorectal Cancer. In *Abeloff's Clinical Oncology (Sixth Edition)*, Niederhuber, J. E.; Armitage, J. O.; Kastan, M. B.; Doroshow, J. H.; Tepper, J. E., Elsevier: Philadelphia, 2020; pp 1219-1280.
56. Dasgupta, A.; Wahed, A., Chapter 13 - Tumor Markers. In *Clinical Chemistry, Immunology and Laboratory Quality Control*, Dasgupta, A.; Wahed, A., Eds. Elsevier: San Diego, 2014; pp 229-247.

57. Gao, Z.; Deng, K.; Wang, X.-D.; Miró, M.; Tang, D. High-Resolution Colorimetric Assay for Rapid Visual Readout of Phosphatase Activity Based on Gold/Silver Core/Shell Nanorod. *ACS Appl. Mater. Interfaces* **2014**, *6*, 18243-18250.
58. Guo, Y.; Wu, J.; Li, J.; Ju, H. A Plasmonic Colorimetric Strategy for Biosensing through Enzyme Guided Growth of Silver Nanoparticles on Gold Nanostars. *Biosens. Bioelectron.* **2016**, *78*, 267-273.
59. Armbruster, D. A.; Tillman, M. D.; Hubbs, L. M. Limit of Detection (LQD)/Limit of Quantitation (LOQ): Comparison of the Empirical and the Statistical Methods Exemplified with GC-MS Assays of Abused Drugs. *Clin. Chem.* **1994**, *40*, 1233-1238.
60. Armbruster, D. A.; Pry, T. Limit of Blank, Limit of Detection and Limit of Quantitation. *The Clinical biochemist. Reviews* **2008**, *29 Suppl 1*, S49-S52.
61. Burns, D. T.; Danzer, K.; Townshend, A. Use of the Term "Recovery" and "Apparent Recovery" in Analytical Procedures (Iupac Recommendations 2002). *Pure Appl. Chem.* **2002**, *74*, 2201.
62. Siekkinen, A. R.; McLellan, J. M.; Chen, J.; Xia, Y. Rapid Synthesis of Small Silver Nanocubes by Mediating Polyol Reduction with a Trace Amount of Sodium Sulfide or Sodium Hydrosulfide. *Chem. Phys. Lett.* **2006**, *432*, 491-496.
63. Xia, X.; Zeng, J.; Oetjen, L. K.; Li, Q.; Xia, Y. Quantitative Analysis of the Role Played by Poly(vinylpyrrolidone) in Seed-Mediated Growth of Ag Nanocrystals. *J. Am. Chem. Soc.* **2012**, *134*, 1793-1801.
64. Frens, G. Controlled Nucleation for the Regulation of the Particle Size in Monodisperse Gold Suspensions. *Nat. Phys. Sci.* **1973**, *241*, 20-22.
65. Gole, A.; Murphy, C. J. Seed-Mediated Synthesis of Gold Nanorods: Role of the Size and Nature of the Seed. *Chem. Mater.* **2004**, *16*, 3633-3640.
66. Ming, T.; Feng, W.; Tang, Q.; Wang, F.; Sun, L.; Wang, J.; Yan, C. Growth of Tetrahexahedral Gold Nanocrystals with High-Index Facets. *J. Am. Chem. Soc.* **2009**, *131*, 16350-16351.
67. Johnson, P. B.; Christy, R. W. Optical Constants of the Noble Metals. *Phys. Rev. B* **1972**, *6*, 4370-4379.
68. Babar, S.; Weaver, J. Optical Constants of Cu, Ag, and Au Revisited. *Appl. Opt.* **2015**, *54*, 477-481.

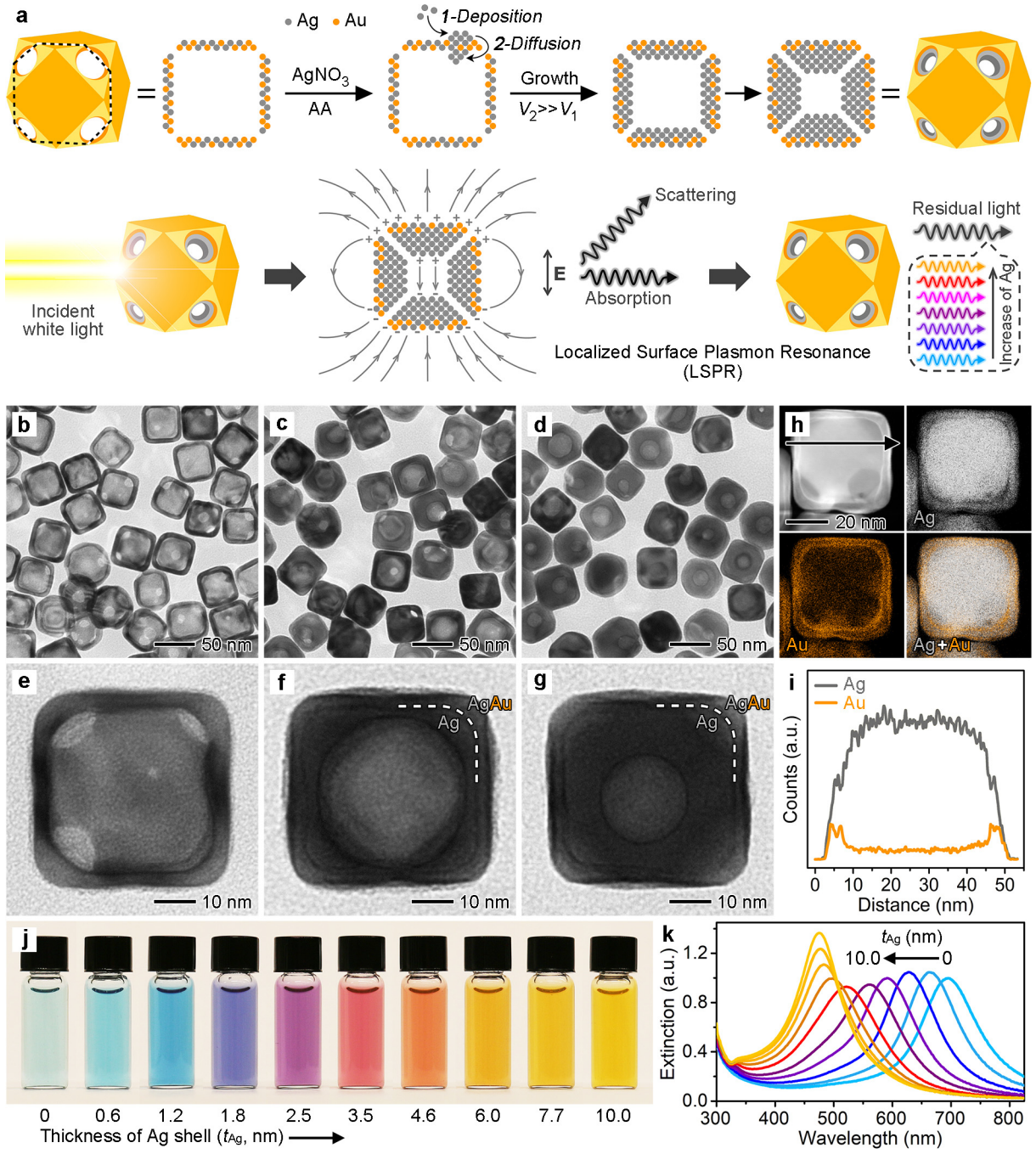


**Figure 1.** Design, characterizations, and LSPR properties of Ag@(Ag-Au) cages. (a) Schematic illustrations showing the synthesis of Ag@(Ag-Au) cages (top trace) and the LSPR extinction of Ag@(Ag-Au) cages with different thicknesses of Ag shells (bottom trace). (b-d) TEM images of Ag@(Ag-Au) cages that were grown from 48 nm Ag-Au cages when 0 μL (b), 8.0 μL (c), and 16.0 μL (d) of $AgNO_3$ had been added. (e-g) Magnified TEM images of samples in (b-d), respectively. (h,i) EDX mapping images (h) and EDX line-scan profiles (i) of the sample shown

in (d). The EDX line-scan profiles were taken from a single nanoparticle shown in (h) along a direction as indicated by the arrow. (j) Photographs taken from aqueous suspensions of Ag@(Ag-Au) cages with different thicknesses of Ag shell in the range of 0-10.0 nm, which were prepared by introducing different volumes of $AgNO_3$ to the growth solution (see METHODS for details). (k) Corresponding LSPR extinction spectra recorded from the samples in (j).

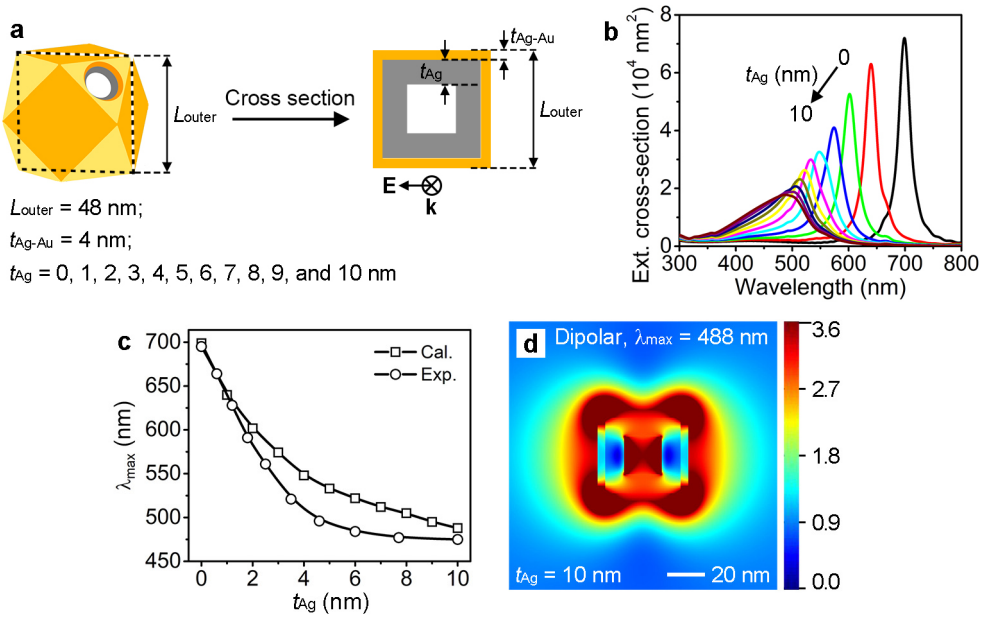


**Figure 2.** FDTD simulations for 48 nm Ag@(Ag-Au) cages with different thicknesses of Ag shell ($t_{Ag}$). (a) Schematics and excitation configuration of the cages. (b) FDTD-simulated extinction cross-section spectra of the cages with $t_{Ag}$ in the range of 0~10 nm. (c) Two curves that were generated by plotting the calculated (Figure 2b) and experimental (Figure 1k) $\lambda_{max}$ against $t_{Ag}$. (d) Electric field intensity map (logarithmic scale) of the cage at $t_{Ag}$ =10 nm. The map was generated at the major LSPR extinction peak at 488 nm.

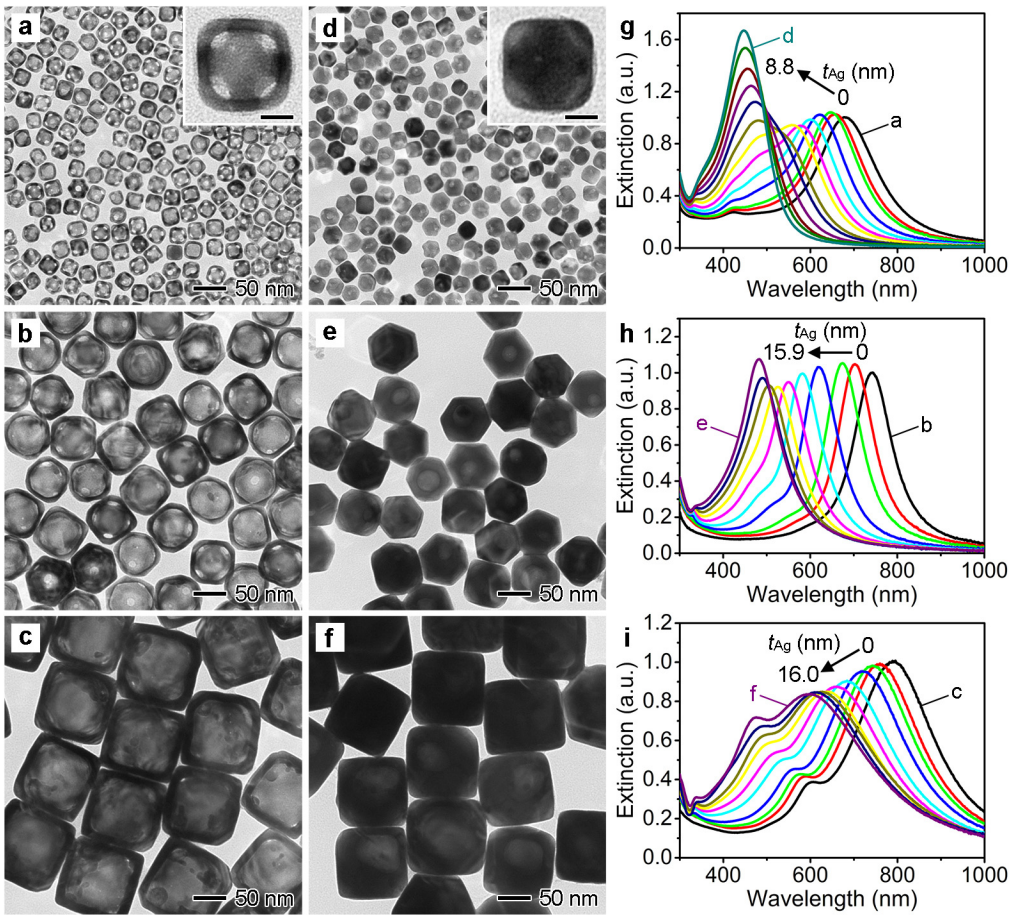


**Figure 3.** Size control of Ag@(Ag-Au) cages. (a-c) TEM images of 27 nm (a), 68 nm (b), and 113 nm (c) Ag-Au cages that were used as seeds for synthesis of Ag@(Ag-Au) cages. (d-f) TEM images of 27 nm (d), 68 nm (e), and 113 nm (f) Ag@(Ag-Au) cages obtained from growth solution of the Ag-Au cages in (a-c), respectively, when 22.0 μL, 16.0 μL, and 28.0 μL of $AgNO_3$ had been introduced. (g-i) LSPR extinction spectra recorded from growth solution of 27 nm (g), 68 nm (h), and 113 nm (i) Ag-Au cages. As indicated by the arrows above the spectra, the thicknesses of Ag shells ($t_{Ag}$) grown inside the 27 nm, 68 nm, and 113 nm cages are in the ranges of 0-8.8 nm (from right to left, $t_{Ag} \approx$ 0, 0.2, 0.3, 0.7, 1.1, 1.5, 2.0, 2.5, 3.1, 3.8, 4.7, 6.0, and 8.8 nm), 0-15.9 nm (from right to left, $t_{Ag} \approx$ 0, 0.5, 1.1, 2.3, 3.7, 5.2, 6.9, 9.0, 11.7, and 15.9 nm), and 0-16.0 nm (from right to left, $t_{Ag} \approx$ 0, 0.4, 0.8, 1.6, 3.4, 5.3, 7.5, 9.9, 12.7, and 16.0 nm), respectively. Insets in (a) and (d) show magnified TEM images of individual cages, where the scale bars are 10 nm. In (g-i), the extinction spectra of samples in (a-f) were labeled.

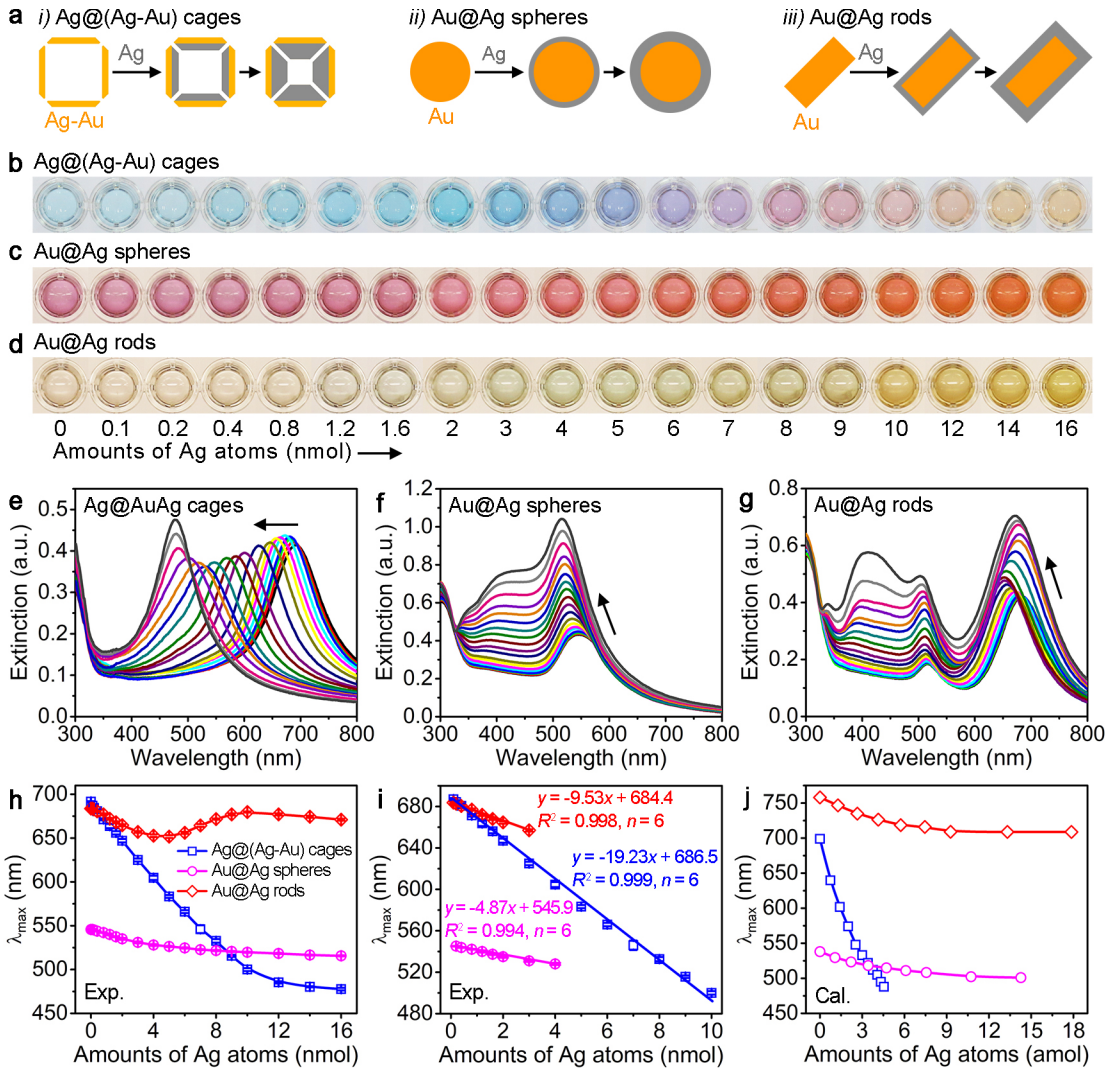


**Figure 4.** Comparison of the LSPR properties of Ag@(Ag-Au) cages, Au@Ag spheres and Au@Ag rods. (a) Schematics showing the synthesis of the three types of nanostructures. The Ag-Au cages (48 nm in edge length), Au spheres (58 nm in diameter), and Au rods (37×90 nm) as seeds correspond to the samples shown in Figures 1b, S12a, and S13a, respectively. (b-d) Representative photographs taken from the growth solutions of Ag-Au cages (b), Au spheres (c), and Au rods (d) as seeds when various amounts of Ag atoms were grown on the seeds. (e-g) LSPR extinction spectra of the solutions shown in (b-d). (h) Corresponding calibration curves of spectra in (b-d), which were obtained by plotting the major LSPR peaks ($\lambda_{max}$) against the amounts of Ag atoms. (i) Linear range regions of the curves shown in (h). (j) Simulated calibration curves that were generated by plotting the simulated $\lambda_{max}$ against the amounts of Ag

atoms grown on individual seeds (see Figures 2a,b, S15, and S16 for the simulation models and results). In (h) and (i), the error bars indicate the standard deviations ($n$ = 6).

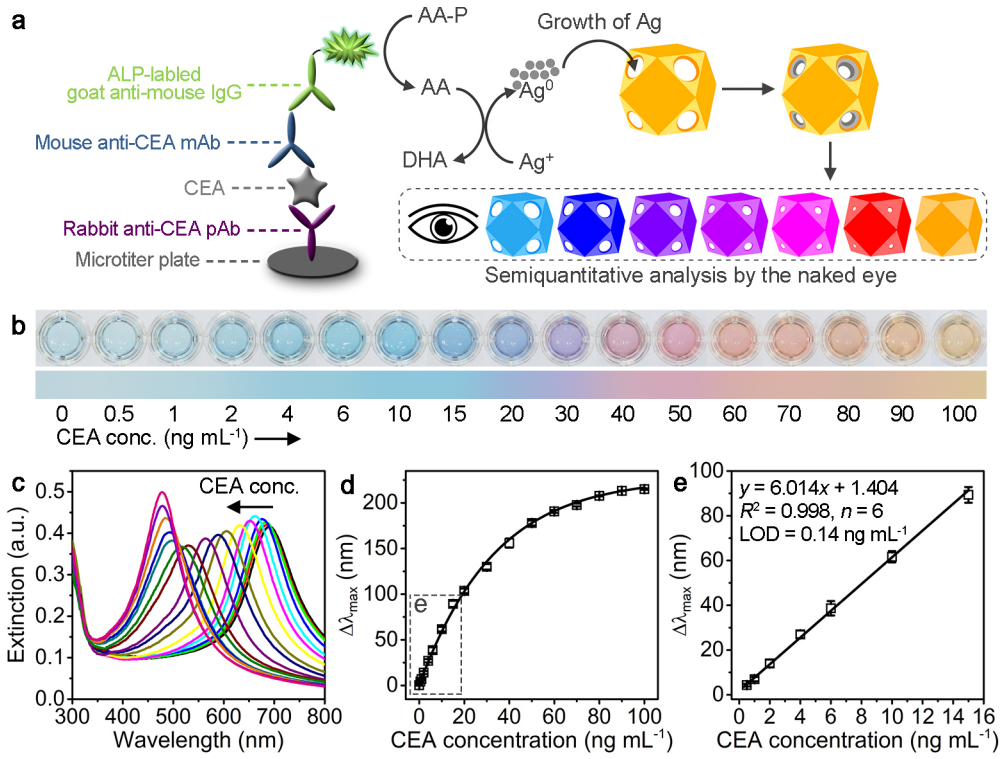


**Figure 5.** Detection of CEA with 48 nm Ag@(Ag-Au) cages-based sensor system. (a) Schematics showing the sensing principle. ALP: alkaline phosphatase; AA-P: L-ascorbic acid 2-phosphate; DHA: L-dehydroascorbic acid. (b) Representative photograph taken from the detection of CEA standards. (c) LSPR extinction spectra of the solutions shown in (b). (d) Corresponding calibration curve generated by plotting the blue shift of major LSPR peak ($\lambda_{max}$) relative to the blank of 0 ng mL$^{-1}$ CEA ($\Delta\lambda_{max}$) against CEA concentration. (e) Linear range region of the curve shown in (d). Error bars indicate the standard deviations ($n$ = 6).

**Table 1.** Analytical performance of 48 nm Ag@(Ag-Au) cages-based sensor in detecting CEA spiked human plasma samples.

| Sample no.[a] | Spiked ($ng\ mL^{-1}$) | Semi-quantitative analysis[b] | | Quantitative analysis[c] | | |
|---|---|---|---|---|---|---|
| | | Color | Found ($ng\ mL^{-1}$) | Found (Mean ± SD) ($ng\ mL^{-1}$) | CVs (%, $n$ = 3) | Recovery (%) |
| 1 | 2 |  | 0~2 | 1.91 ± 0.24 | 12.6 | 95.3 |
| 2 | 10 |  | ~10 | 10.55 ± 0.89 | 8.4 | 105.5 |
| 3 | 25 |  | ~30 | 26.90 ± 1.28 | 4.8 | 107.6 |
| 4 | 50 |  | 40~50 | 48.93 ± 2.32 | 4.7 | 97.9 |
| 5 | 100 |  | ~100 | 93.01 ± 4.70 | 5.1 | 93.0 |

[a]Each sample was analyzed by three times in parallel. [b]Semi-quantitative analysis was performed based on the color chart of CEA standards as shown in Figure 5b. [c]Quantitative analysis was performed based on the calibration curve shown in Figure 5e. SD and CV stand for standard deviation and coefficient of variation, respectively.